A wavelength-induced frequency filtering method for fluorescent nanosensors in vivo

Volodymyr B. Koman [1,6], Naveed A. Bakh[1,6], Xiaojia Jin [1], Freddy T. Nguyen [1,2,3], Manki Son[1], Daichi Kozawa[1,4], Michael A. Lee[1], Gili Bisker [5], Juyao Dong[1] and Michael S. Strano [1]✉

Fluorescent nanosensors hold the potential to revolutionize life sciences and medicine. However, their adaptation and translation into the in vivo environment is fundamentally hampered by unfavourable tissue scattering and intrinsic autofluorescence. Here we develop wavelength-induced frequency filtering (WIFF) whereby the fluorescence excitation wavelength is modulated across the absorption peak of a nanosensor, allowing the emission signal to be separated from the autofluorescence background, increasing the desired signal relative to noise, and internally referencing it to protect against artefacts. Using highly scattering phantom tissues, an SKH1-E mouse model and other complex tissue types, we show that WIFF improves the nanosensor signal-to-noise ratio across the visible and near-infrared spectra up to 52-fold. This improvement enables the ability to track fluorescent carbon nanotube sensor responses to riboflavin, ascorbic acid, hydrogen peroxide and a chemotherapeutic drug metabolite for depths up to 5.5 ± 0.1 cm when excited at 730 nm and emitting between 1,100 and 1,300 nm, even allowing the monitoring of riboflavin diffusion in thick tissue. As an application, nanosensors aided by WIFF detect the chemotherapeutic activity of temozolomide transcranially at 2.4 ± 0.1 cm through the porcine brain without the use of fibre optic or cranial window insertion. The ability of nanosensors to monitor previously inaccessible in vivo environments will be important for life-sciences research, therapeutics and medical diagnostics.

Apart from their therapeutic use, nanoparticles in the form of fluorescent nanosensors hold great potential in life-sciences and clinical research[1–3]. High-throughput screening using fluorescent nanosensors and probes has enabled the preclinical evaluation and clinical trials of drug efficacy[4], biodistribution[5] and pharmacokinetics[6]. Fluorescent nanosensors can also aid in the early detection of arthritis[7], viral infections[8], cardiovascular[9] and inflammatory diseases[10], as well as cancer and metastasis[11,12]. The nanosensors are also considered potent tools for the early detection of biomarkers, for providing kinetic information on disease progression and response to therapeutics[13,14]. However, the vast majority of nanosensor studies are performed either in vitro or, in some instances, with nanosensors implanted in superficial tissue layers at depths of a few millimetres. Potentially translating the large number of florescent nanosensors to animal and human in vivo studies requires substantially deeper sensor implantation, motivating the need for novel photonic or spectroscopic solutions. In this work, we develop wavelength-induced frequency filtering (WIFF) as a technique to detect optical emission from fluorescent nanosensors deeply embedded within strongly scattering tissue. WIFF modulates the excitation wavelength across the absorption peak of a nanosensor to separate the autofluorescence background, increasing the signal-to-noise ratio (SNR) and drastically reducing noise levels. These aims and applications are distinct from the problem of improved spatial resolution as in bioimaging[15].

A few recent studies have improved SNR for in vivo fluorescence sensing using a variety of hardware and materials science approaches. Among them, gastric pH sensing has been demonstrated in the stomach of ICR mice using molecular fluorophores with up to 4 mm penetration depth and 84 μm spatial resolution[16]. As the implantation depth increases, spatial information is scrambled and the total signal attenuates. To maximize the SNR, one study only assessed the cumulative signal intensity when measuring the pH levels and oxygen contents using polymer–iridium probes in the mammary glands of nude mice[17]. Using co-polymer hydrogels, another study demonstrated subcutaneous glucose sensing at 5 mm depth in a porcine model[18]. The rapid kinetics of histamine using subcutaneously injected ionophore sensors in mice was also reported[19]. Several studies explored the limits of deep implantation[20–22], particularly with 3.2 cm depth in porcine tissue achieved using $NaYbF_4$ upconversion nanoparticles[22]. However, these results focused on spatially localizing the probe and not on low-noise temporal signal transmission as one needs for optical sensing at extreme depths. Carbon nanotubes were used to measure nitric oxide in mouse liver[23], but they worked either with extracted organs or optical windows for in situ measurements to circumvent the limitations associated with thick tissue. Similarly, a fibre optic sensor was used to detect morphological and biochemical species within the coronary arteries of swine[24] to solve the problem of optical transmission through the tissue itself. Although several works have investigated factors limiting the performance of fluorescent nanosensors in vivo (Supplementary Note 1), to date, no technique exists, to the best of our knowledge, to detect a fluorescent signal at high fidelity from a nanosensor implanted deep into the tissue.

Here we introduce WIFF to extend the application of fluorescent nanosensors in vivo for biomedical applications. WIFF modulates
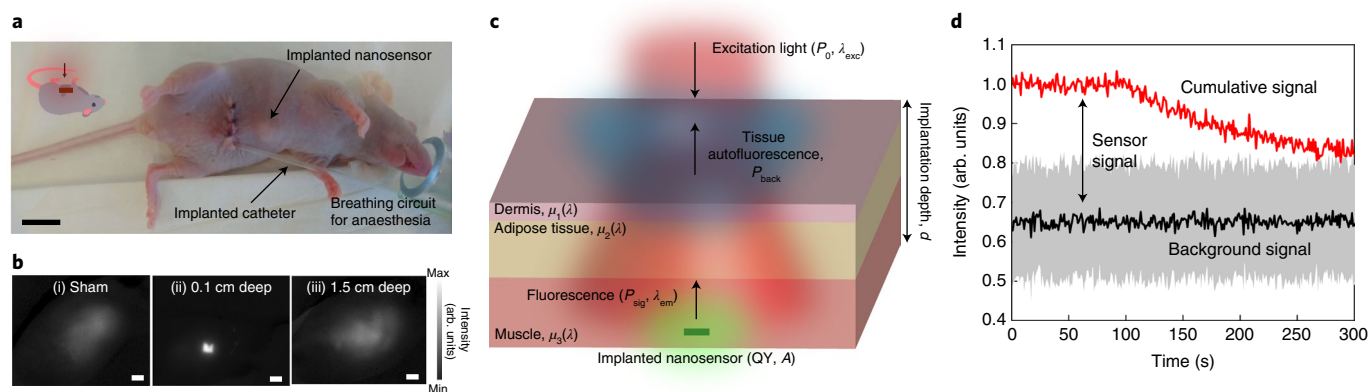
Fig. 1 | Challenges for deep-tissue sensing. a, Photograph of an SKH1-E mouse under anaesthesia with an implanted nanosensor (subcutaneous $5 \times 5 \times 2$ mm³ hydrogel with 20 mg l⁻¹ $(AC)_{15}$-SWNTs) and an implanted catheter used to deliver analytes. Scare bar, 1 cm. **b,** Near-infrared images of subcutaneously implanted $5 \times 5 \times 2$ mm³ hydrogels: sham (an implant without a nanosensor) (i), 0.1-cm-deep nanosensor (a hydrogel with 20 mg l⁻¹ $(AC)_{15}$-SWNTs) (ii) and 1.5-cm-deep nanosensor (the same implant as in (ii), but with a mouse flipped on the other side) (iii). Scale bars, 1 cm. The experiments were repeated over $n = 5$ biologically independent samples. **c,** Schematic of excitation light (red) penetrating through a three-layered tissue to excite an implanted nanosensor. Tissue autofluorescence (blue) and laser reflection compete with the nanosensor emission (green). **d,** Normalized fluorescence intensity from a nanosensor ($5 \times 5 \times 2$ mm³ hydrogel with 20 mg l⁻¹ $(AC)_{15}$-SWNTs) implanted 1.5 cm deep inside a mouse after 100 μl riboflavin (300 μM) injection at $t = 0$ through the catheter. The red line represents a signal stemming from the sensor and the intrinsic autofluorescence background, whereas the black line represents the background with its standard deviation as measured before nanosensor implantation ($n = 5$).

the fluorescence excitation wavelength across the absorption peak of a nanosensor to separate the autofluorescence background, increase the SNR and reduce the noise levels. This allows us to experimentally improve the SNR by up to 52-fold compared with the case without WIFF and to recover signals from depths up to 5.5 ± 0.1 cm in chicken breast tissue using carbon nanotubes as a model nanosensor excited at 730 nm and emitting in the 1,100–1,300 nm range. WIFF utilizes a single-channel detector to maximize signal collection, not addressing spatial resolution as in bioimaging. WIFF has been extensively tested and validated using probes that absorb across a broad spectral range and in several complex tissue types, including widely employed phantom tissues, foetal pig model of composite tissues and live SKH1-E mice. We further use a separated autofluorescence background as an internal reference, a feature valuable for successfully correcting for tissue movement. Such self-referencing enables WIFF to track real-time nanosensor responses to riboflavin, ascorbic acid and hydrogen peroxide from deep nanosensor implants within living SKH1-E mice and preserved foetal pigs at high fidelity with 2.5 Hz temporal resolution, also enabling new tissue permeability measurements of the intraperitoneal cavity. As an application, nanosensors aided by WIFF perform the transcranial monitoring of a metabolite product of temozolomide (TMZ) drug without the use of fibre optic or cranial window insertion, measuring local permeability values of brain tissue up to a depth of 2.4 cm—a milestone, to the best of our knowledge, that has not been demonstrated from any existing method in biomedical optics.

WIFF separates nanosensor signal and background

Light decays exponentially through biological tissue, imposing a substantial limit on the detection depth. The near-infrared fluorescence image of a subcutaneously implanted model nanosensor, in the form of a biocompatible hydrogel containing single-walled carbon nanotubes (SWNTs)[25,26], in an SKH1-E mouse (Fig. 1a,c) is readily visible from the site of implantation (Fig. 1b(ii)) 1 mm deep. The signal, however, vanishes when detected through a 1.5 cm optical path (Fig. 1b(iii)), becoming indistinguishable from the autofluorescence and scattering background of a sham implant (Fig. 1b(i)). As the spatial information from deep implantation sites is lost due to intrinsic tissue scattering, this work utilizes a single-channel detector to collect the signal, minimizing noise that arises from

spreading light over the camera pixels (Methods). To accurately assess the sensor signal, one needs to subtract the background signal (Fig. 1d); yet, the latter is associated with large errors caused by animal movements and precise positioning (as shown later). This procedure severely undermines the measurement accuracy, especially in deep-tissue sensing where a background surpasses the sensor signal by many times.

To lower the noise level, we introduce WIFF. WIFF targets a broad pool of fluorescent nanosensors whose fluorescence changes on the reaction with an analyte but their absorption remains constant[26,27]. WIFF oscillates the excitation wavelength around the nanosensor absorption peak with a constant frequency f (Fig. 2a). This excitation profile produces a nanosensor emission signal that oscillates at $2f$, whereas any monotonous background in this range will have a dominant f component that is easily filtered. The technique relies on the difference between the nanosensor and background absorption peaks. We graphically illustrate the effect (Fig. 2a and Supplementary Fig. 1). The resulting emission intensity can be found at the intersection of the excitation wavelength trace and absorption spectrum, whereas the emission spectral ranges of a sensor and background overlap (Fig. 2b,c). A sweep in excitation wavelength leads to a peak in the nanosensor signal and a monotonic trace in the background. Hence, continuously oscillating the excitation wavelength produces twice as many peaks in the nanosensor signal as the background (Fig. 2d,e). This principle allows WIFF to separate the overlapping nanosensor and background signals in the frequency domain.

The main technical challenge associated with the experimental implementation of WIFF lies in the ability to perform wavelength modulation with amplitudes comparable to the absorption linewidths and repetition rates fast enough to capture the sensor dynamics. Currently, tunable lasers and filters provide milliseconds of tuning times for megahertz wavelength ranges that are used in probing narrow gas absorption lines[28]. For fluorescent nanosensors that typically have their absorption lines in the range of 20–50 nm, the tuning times are limited to a few seconds. To implement WIFF, we developed a system based on three lasers with equally spaced wavelengths and mechanical shutters programmed to open sequentially (Fig. 2f and Supplementary Fig. 2). As a result, our setup allows changing the excitation wavelengths that are
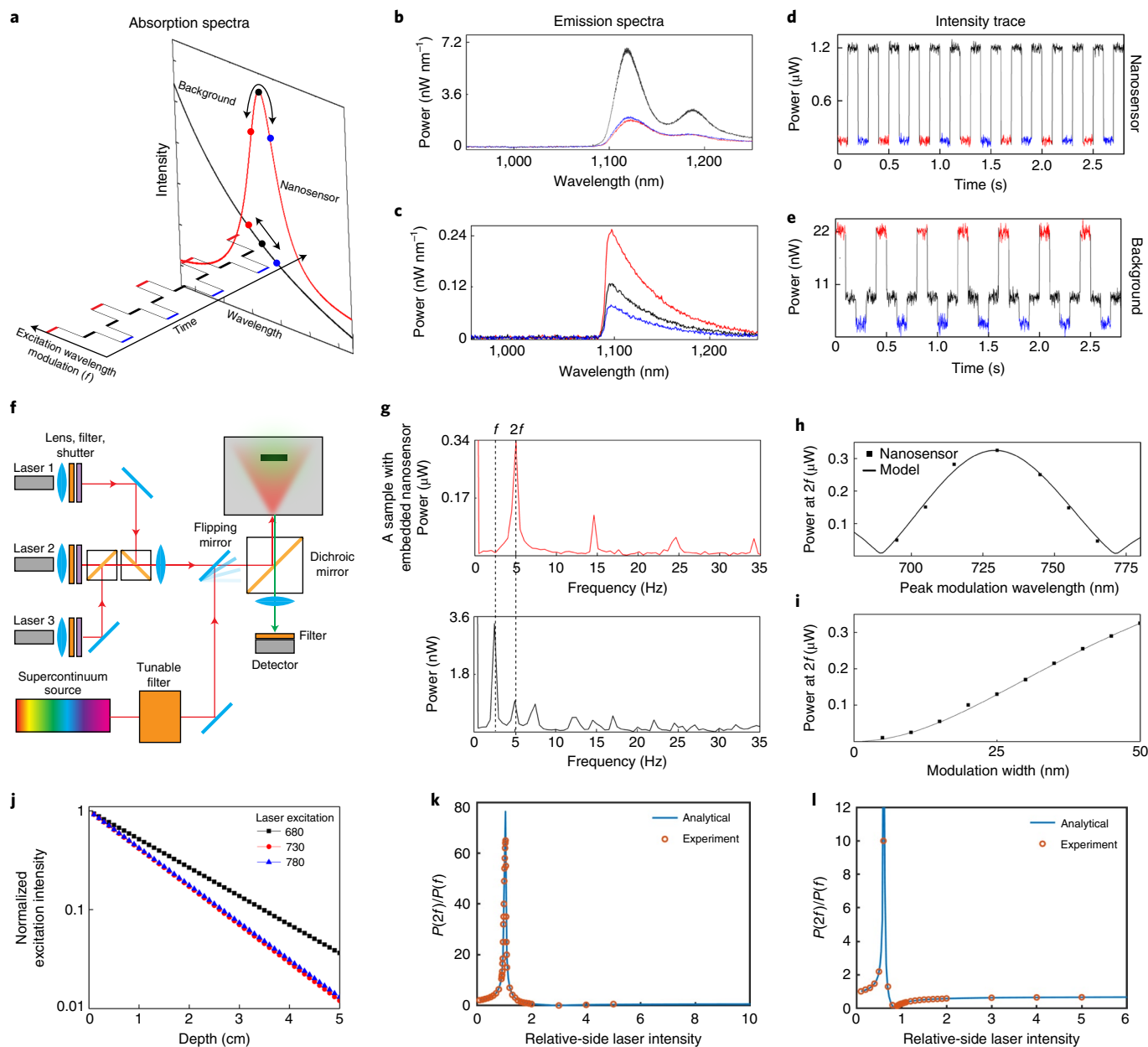
Fig. 2 | Principle of WIFF. a, Graphical depiction of the WIFF principle where the wavelength of excitation light is modulated at frequency *f* around a nanosensor absorption peak, whereas the background has a monotonic spectrum in the same region. **b,** Experimentally measured emission spectra (with 1,100 nm long-pass filter) of a nanosensor (5×5×2 mm³ gel with 10 mg l⁻¹ (GT)₁₅-SWNTs) probed with three lasers used in WIFF excitation: 680 nm (red), 730 nm (black) and 780 nm (blue) operated at 300 mW cm⁻². **c,** Same as in **b**, but for the background (5×5×5 cm³ phantom tissue). **d,e,** Resulting intensity traces when the emission is collected by one channel detector for the nanosensor (**d**) and the background (**e**) demonstrate the emitted signal that oscillates at 2*f*, whereas the background emission at *f*. The colours correspond to laser excitations as above. **f,** Schematic of the experimental setup for three-laser wavelength modulation. The excitation is programmed via a sequential opening of three mechanical shutters in front of the lasers, achieving a profile as that in **a**. **g,** FFT spectra extracted from **d** (top) and **e** (bottom) demonstrate that the signal and background can be separated using WIFF. **h,i,** Intensity of the 2*f* component measured for different excitation peak wavelengths (**h**) and modulation widths (**i**). The points refer to experimental measurements, whereas lines show the analytical model (described in the main text). **j,** Monte Carlo simulations of the normalized light intensity travelling through phantom tissue for three excitation wavelengths. The intensity of the 680 nm laser needs to be corrected by almost three times at 5 cm implantation. **k,** Ratio of the 2*f* and *f* components for a sensor (5×5×2 mm³ gel with 10 mg l⁻¹ (GT)₁₅-SWNTs) as a function of the side laser intensity (680 nm) compared with the central laser intensity (730 nm). **l,** Ratio of the 2*f* and *f* components for the background autofluorescence stemming from the phantom tissue.

50 nm apart faster than 10 Hz to collect up to 15% of the signal in the 2*f* component with other modulation schemes less effective (Supplementary Fig. 3).

The experimental implementation of WIFF uses three lasers (680, 730 and 780 nm) that excite a fluorescent nanosensor in a stepwise manner at *f* = 2.5 Hz and a single-channel detector to collect the emitted fluorescence (Fig. 2f). We use WIFF in addition to the commonly employed intensity modulation scheme, where the two techniques are orthogonal in their implementations and purposes (Methods). As evident from the time traces (Fig. 2d,e) and
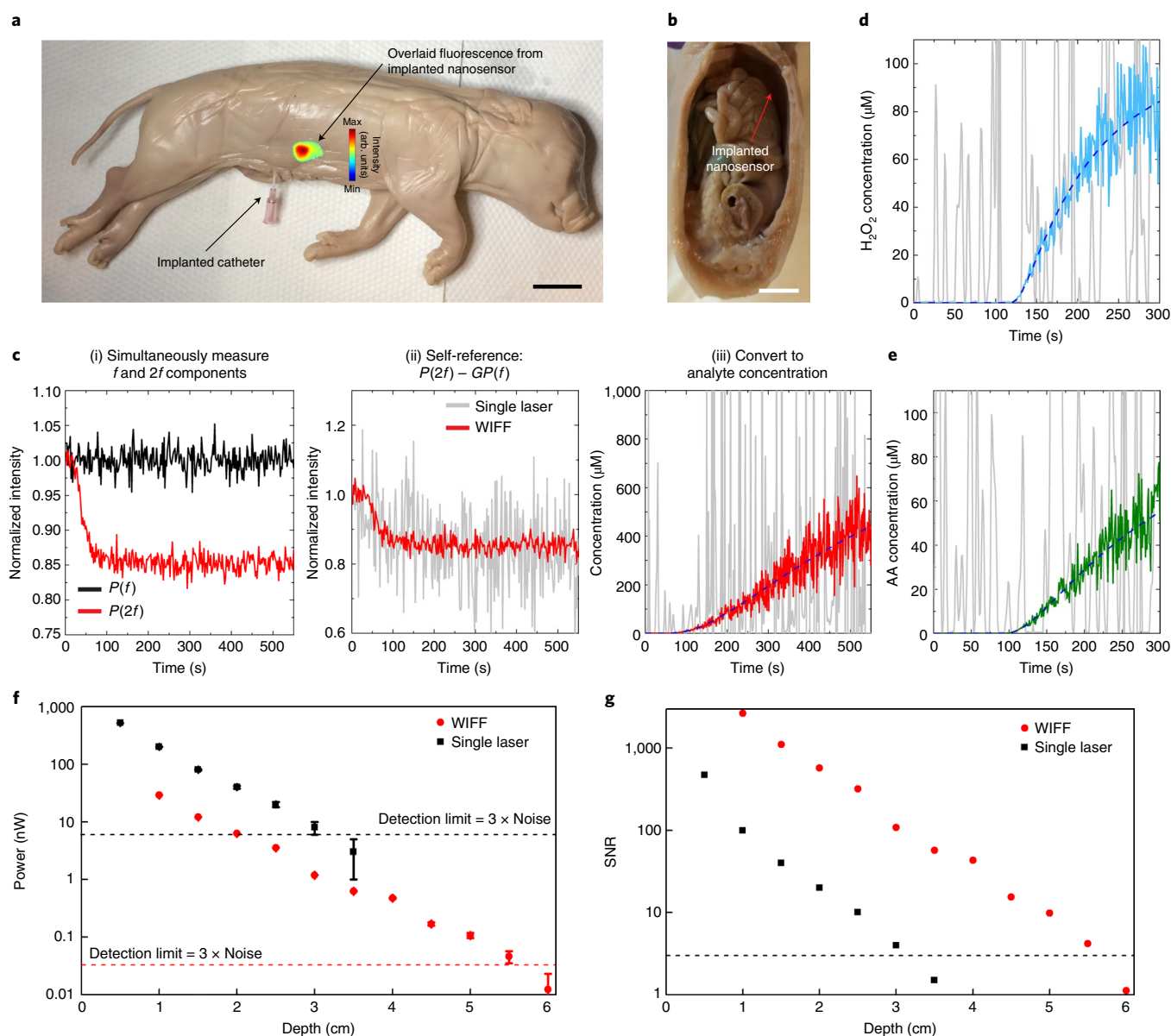
Fig. 3 | WIFF performance in a complex tissue. a, Photograph of a preserved foetal pig with a nanosensor ($10 \times 10 \times 2$ mm³ hydrogel with 20 mg l⁻¹ (AC)₁₅-SWNTs) implanted into the intraperitoneal space. A photograph is overlaid with a near-infrared image of the implanted nanosensor. Scale bar, 2.5 cm. **b**, Cross-sectional view of the preserved foetal pig demonstrating the intraperitoneal space where the nanosensor was implanted. Scale bar, 1 cm. **c**, Steps for WIFF: simultaneous tracking of f and $2f$ components of the signal on the injection of 3 ml of 1 mM riboflavin at $t = 0$ through the implanted catheter (i). The measurements were performed on the pig's side opposite to the nanosensor implantation, corresponding to 2.3 cm implantation depth. WIFF self-referencing reveals the nanosensor response overlaid with the signal from the single-laser excitation scheme (ii). WIFF data translated into actual riboflavin concentration as fitted to a model of analyte diffusing into the hydrogel (dashed blue) (iii). **d,e**, Similarly extracted hydrogen peroxide (H_2O_2) (**d**) and ascorbic acid (AA) (**e**) concentrations for nanosensors ($10 \times 10 \times 2$ mm³ hydrogel with 20 mg l⁻¹ (GT)₁₅-SWNTs and (ACCA)₇-SWNTs) implanted at 3 cm depth in phantom tissue on the addition of 100 μM analytes at 106 and 81 s, respectively. **f,g**, The signal (**f**) and its SNR (**g**) for a nanosensor ($5 \times 5 \times 2$ mm³ gel with 10 mg l⁻¹ (GT)₁₅-SWNTs) implanted at various depths into the chicken breast tissue. The error bars represent standard deviation over $n = 5$ independent samples. The dashed line in **g** corresponds to an SNR of 3. The nanosensor signal was found as the difference between two measurements from a sample with and without a sensor. The single-laser excitation was set at 730 nm. The WIFF system was modulated at 2.5 Hz among 680, 730 and 780 nm. The emission collection was set at >1,100 nm.

Fourier analysis (Fig. 2g), this excitation drives the fluorescence signal at $2f$, whereas the background has a dominant f component, separating the two. In our system, mechanical artefacts caused by shutter vibrations become considerable above 5 Hz modulation (Supplementary Fig. 4), limiting the modulation speed of the setup; yet, this occurs well above the dynamics of various biomedical

processes[23]. Approximating the absorption profile of the nanosensor with a Lorentzian lineshape, the fluorescent signal P_s can be expressed as (Supplementary Fig. 5)

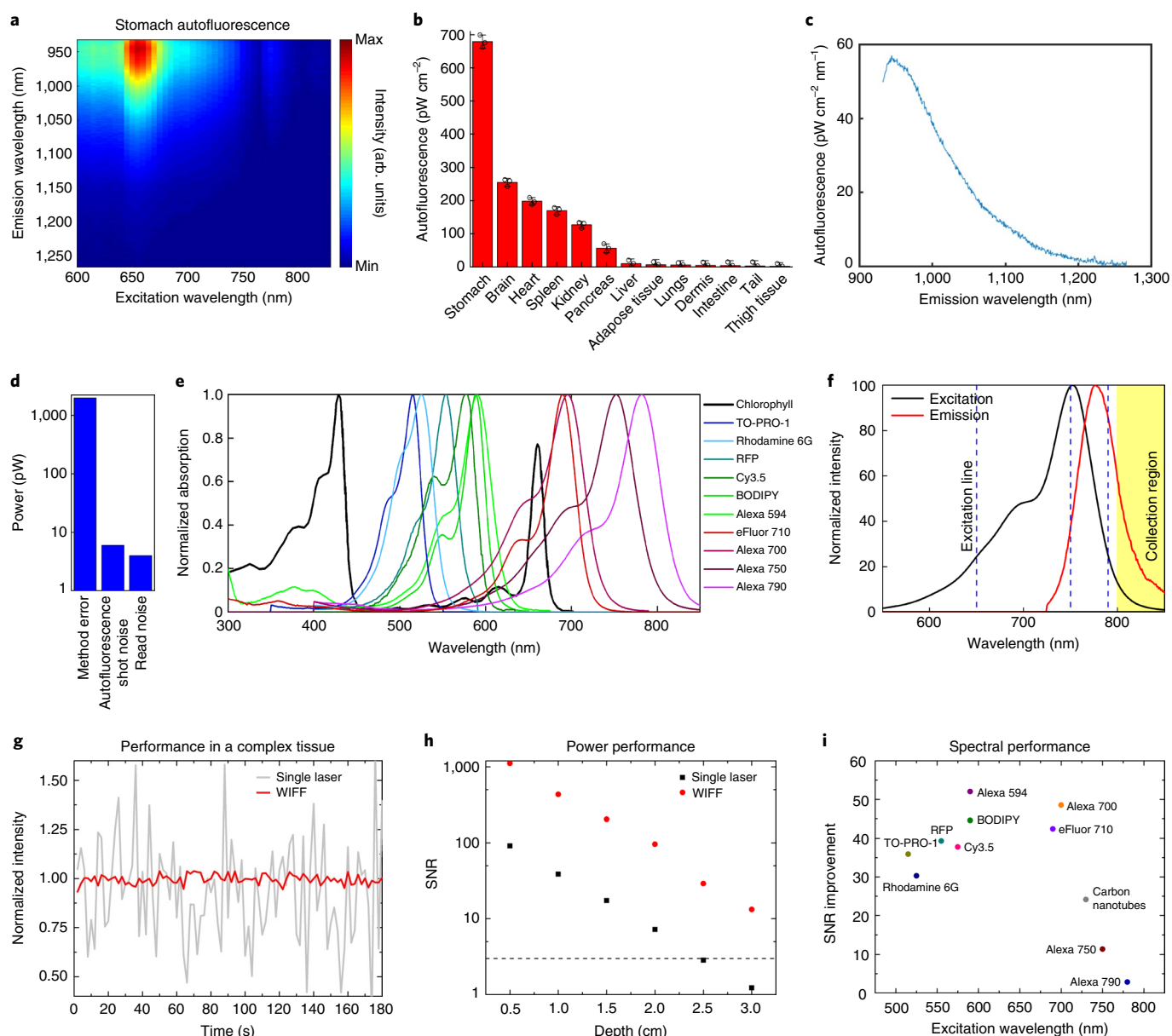$$P_s(\lambda) = A \frac{1}{(\lambda - \lambda_{11})^2 + \gamma^2}, \quad (1)$$

Fig. 4 | Elucidating the effect of autofluorescence on WIFF and deep-tissue detection. a, Excitation–emission map for a freshly killed SKH1-E mouse stomach. **b**, Summary of autofluorescence intensity for various mice organs at 1.7 mW cm⁻² power of 730 nm excitation and infrared emission (>1,100 nm). All the organs listed after pancreas had autofluorescence signal below the detection limit. The error bars represent standard deviation over $n = 3$ biologically independent samples. **c**, Emission line extracted from **a** for 730 nm excitation. **d**, Estimated noise levels. **e**, Normalized absorption spectra of chlorophyll and ten fluorophores. **f**, Normalized absorption (black) and emission (red) spectra for Alexa 700 fluorophore. The dashed blue lines correspond to excitation lines and the yellow-shaded region corresponds to the collection range. **g**, Normalized intensity for a single laser and WIFF traces for a fluorophore (10 μM Alexa 594 in a 10 × 20 × 2 mm³ dialysis bag) subcutaneously implanted on the ventral side of a preserved foetal pig. **h**, SNR values for a fluorophore (2 μM Alexa 750 in a 5 × 5 × 2 mm³ chamber) implanted at various depths inside the phantom tissue ($n = 3$). The dashed line corresponds to an SNR of 3. **i**, SNR improvement when using WIFF over the single-laser excitation scheme for various fluorophores implanted at 1 cm depth of phantom tissue.

where A is an amplitude constant; λ and λ_{11} are the excitation and peak centre wavelengths, respectively; and γ is another constant that determines the peak linewidth. The background signal P_b can be approximated as (Supplementary Fig. 6)

$$P_b(\lambda) = B\exp\left[-\alpha(\lambda - \lambda_0)\right], \qquad (2)$$

where B and α are fitting parameters (found to be 0.02 for SKH1-E mouse tissues in the 680–800 nm region) and λ_0 is the absorption peak of autofluorescence (taken to be 655 nm). Expanding equations (1) and (2) into a Taylor series and taking the Fourier transform,

expressions for signal harmonics can be found (Supplementary Figs. 5 and 7 and Supplementary Note 2). It can be further shown that a ratio between the background f and $2f$ components, namely,

$$G = \frac{P_b(2f)}{P_b(f)}, \qquad (3)$$

depends only on the spectral shape of tissue autofluorescence and excitation modulation, but is invariant to the excitation power or collection efficiency. For the modulation width of 50 nm, we estimate G being 0.27 for SKH1-E mouse tissues (Supplementary Fig. 6).

Although different organs have some variations in absorption profiles, G remains constant for whole-animal experiments when measured from the animal side, as shown below (Supplementary Table 1). Assuming that our nanosensor provides no f component (or it is very low compared with that of the background), we can effectively filter out the background contribution to the signal:

$$P_{\text{WIFF}} = |P_{\text{s+b}}(2f) - GP_{\text{s+b}}(f)|. \tag{4}$$

Equation (4) allows performing self-referenced measurements where the $2f$ component is corrected by the f component that mostly bears the background signal.

To understand the limits of WIFF application, we employed a supercontinuum laser with a tunable filter to tune the wavelength modulation excitation (this source allows for greater tunability, but with much lower modulation frequencies of only 0.1 Hz). The intensity of the $2f$ component strongly depends on the excitation wavelength and, as expected, peaks at the absorption maximum (Fig. 2h, Supplementary Fig. 8 and Supplementary Note 3). Both modulation width (Fig. 2i and Supplementary Fig. 9) and narrow laser linewidth (Supplementary Fig. 10) further increase the $2f$ component. To minimize the background $2f$ component, the spectral distance between the background and signal absorption peaks needs to exceed the modulation width (Supplementary Fig. 11). Finally, the excitation wavelengths themselves exhibit different tissue absorption levels that distort the modulation pattern (Fig. 2j). This effect depends on the implantation depth and tissue absorption profile and is mitigated by correcting the relative laser intensities to maximize the $2f$ component of a sensor (Fig. 2k). Such correction leads to changes in the background signal (Fig. 2l) to be accounted for with the updated G factor.

WIFF enables deep-tissue sensing

To demonstrate how WIFF increases the SNR and improves the sensing capabilities operating in complex tissues, we implanted model fluorescent nanosensors into the intraperitoneal space from the ventral side of preserved foetal pigs (Fig. 3a,b). The intraperitoneal space is often used for injections in veterinary medicine[29] as well as for the administration of chemotherapeutic drugs in humans[30]. In this geometry, light has to travel through layers of tissue and fluids with various refractive indexes (such as dermis, adipose, muscle and peritoneum) to reach the implant. Throughout this work, we will utilize preserved foetal pigs as an animal model that captures all the intricacies of light penetration, yet minimizes the number of experiments on live animals. As an example, we use a carbon nanotube sensor tailored for the selective detection of riboflavin (Methods), a vitamin that can be administered in case of its deficiency[31], with sensitivities down to 10 nM concentrations[32]. On a 3 ml injection of 1 mM riboflavin through a catheter implanted in the vicinity of the nanosensor, WIFF measurements revealed quenching of the signal's $2f$ component, whereas the f component's time trace remained invariant (Fig. 3c(i)). Using equation (4), WIFF then separates the nanosensor contribution from that of the background. Earlier measurements on specimens without a sensor yield the G factor (equation (3)) of the tissue to be 0.29 ± 0.01 (in agreement with theoretical predictions). As a result, we measured an $18 \pm 1\%$ nanosensor quenching response at a substantial implant depth of 2.3 ± 0.1 cm (Fig. 3c(ii)) compared with control injections of saline that remained invariant (Supplementary Fig. 12). Similar results were obtained across $n = 5$ replicas (Supplementary Figs. 13 and 14) to be further converted into actual riboflavin concentrations using a calibration curve (Fig. 3c(iii)) (red line), Supplementary Note 4 and Supplementary Table 2) with examples of processing steps provided in Supplementary Figs. 15 and 16. From the same dataset, we also compare WIFF with standard fluorescence geometry, where excitation is performed by a single laser with the same excitation

power as WIFF and the excitation wavelength corresponding to the absorption peak of the nanosensor. At shallow sensor implantation, WIFF and single-laser excitation produce similar sensor responses (Supplementary Fig. 17), validating the WIFF capabilities. For deep implantations, the single-laser approach yields a prohibitively low SNR value for the extracted concentration to reveal any meaningful information (Fig. 3c(iii), black line). Importantly, WIFF represents a general method extendable to a wide range of nanosensors. For instance, WIFF produced similar results using nanosensors for H_2O_2 (Fig. 3d and Supplementary Fig. 18), an oxidative stress marker and a signalling molecule[33], as well as ascorbic acid (Fig. 3e and Supplementary Fig. 19), a vitamin and an essential nutrient[27].

By significantly reducing noise levels, WIFF allows detecting implant signals from several centimetres deep—thicknesses comparable to those needed to monitor biochemical environments in multiple organs of the human body[23]. To illustrate this, we applied WIFF to nanosensors implanted at different depths into chicken breast tissue (Fig. 3f) and phantom tissue (Supplementary Fig. 20). These tissues were selected because they afford the ability to precisely control the implantation depth in these experiments as well as their homogeneous optical properties that enable a direct comparison of performance. Single-laser measurements demonstrate that the signal drops exponentially with an attenuation coefficient of 1.62 cm^{-1} (1.76 cm^{-1}) for chicken breast tissue (phantom tissue). Photomigration Monte Carlo simulations of light propagation in simulated random media were compared with these data, verifying the absence of spurious reflections that would exhibit deviations from exponential scaling (Supplementary Fig. 21). At a depth of 3.2 cm (2.9 cm) for chicken breast tissue (phantom tissue), the signal dropped to several nanowatts with SNR being close to 3, reaching the limit of detection[34]. The application of WIFF reduced the noise level by 182 times from 2 nW to 11 pW, approaching the read noise of the detector. This improvement yielded a 27-fold SNR increase over the case of single-laser excitation (Fig. 3g). This SNR boost enabled the ability to pick up nanosensor signals from extremely deep implants, up to 5.5 ± 0.1 cm in chicken breast and 4.8 ± 0.1 cm in phantom tissue.

WIFF broad spectral range

To quantitatively understand the role of tissue autofluorescence on WIFF performance, we measured the autofluorescence background in the near-infrared range from 12 organs of freshly killed SKH1-E mice. Mice on alfalfa-rich diets were chosen because of their ubiquitous use in biomedical research. Profiles from all the organs (Fig. 4a and Supplementary Fig. 22) display a strong band at around 650 and 950 nm emission—a feature partially attributed to chlorophyll (Supplementary Fig. 23)[35]. Unsurprisingly, we found the digestive organs to exhibit the highest autofluorescence, but the brain and heart ranked second and third in intensity, respectively (Fig. 4b). Because of this, an alfalfa-free diet can significantly reduce organ autofluorescence in mice[36]. The autofluorescence band has a spectral tail that extends up to 1,200 nm and therefore even interferes with near-infrared probes (Fig. 4c). A nanosensor signal itself does not determine the limit but rather the SNR, where autofluorescence contributes to various noises (Supplementary Fig. 24 and Supplementary Note 5).

The noise level of 2 nW extracted from measurements (Fig. 3) was found to be significantly higher (Fig. 4d) than the autofluorescence shot noise (estimated to be 6 pW) and the read noise of our detector (root mean square (r.m.s.) value of 4 pW). The required background subtraction for this measurement manifests in the method error as the nanosensor signal P_s is computed as the difference between two measurements—with ($P_{\text{s+b}}$) and without (P_b) an implanted nanosensor:
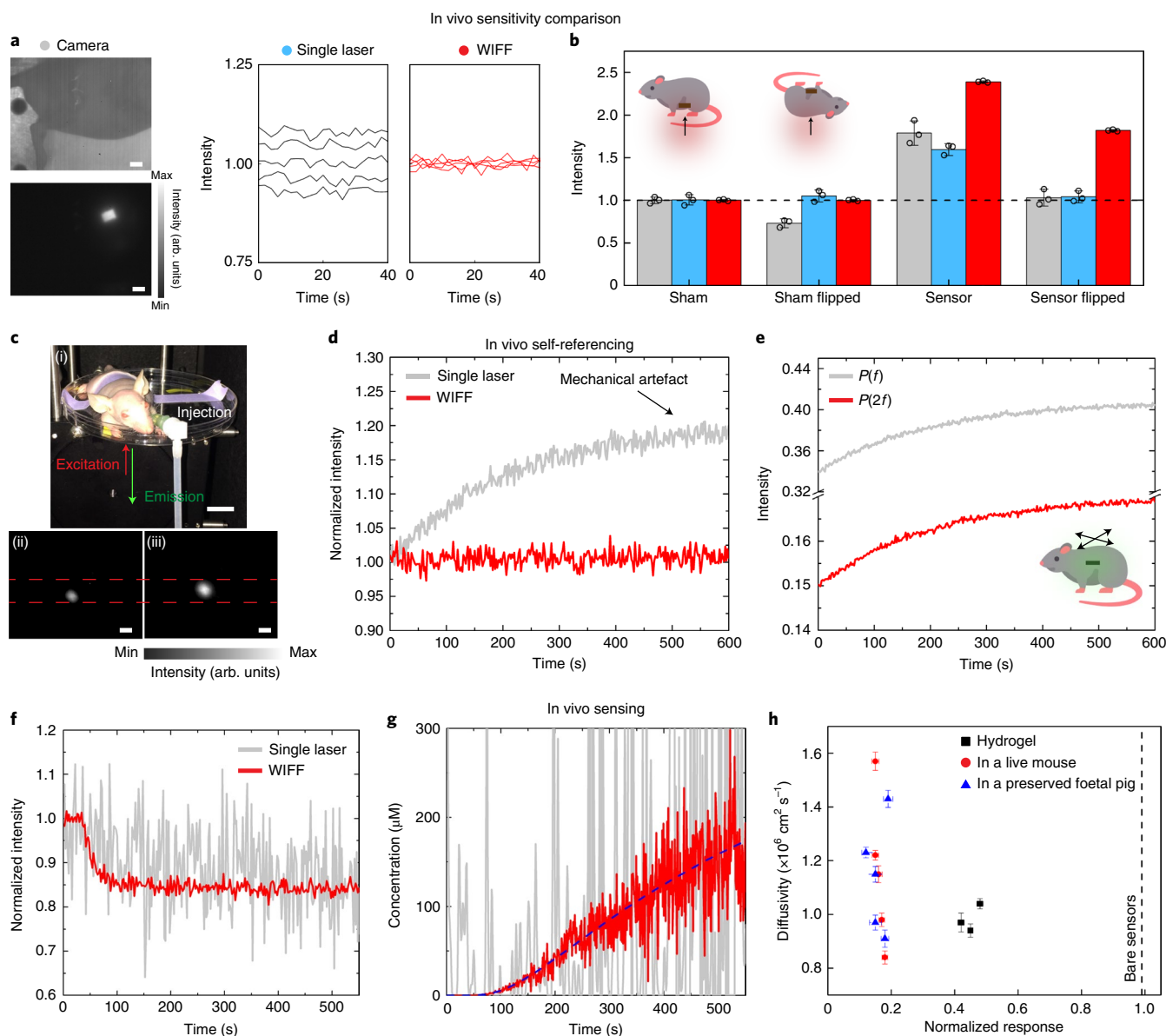
$$P_s = P_{\text{s+b}} - P_b. \tag{5}$$

Fig. 5 | In vivo sensing. a, Photograph of an SKH1-E mouse with a nanosensor ($5 \times 5 \times 2$ mm^3 hydrogel with 20 mg l^{-1} (AC)$_{15}$-SWNTs) subcutaneously implanted near the stomach area, the respective near-infrared image and single-laser and WIFF measurements of the sensor signals ($n = 5$ biologically independent samples). Scale bars, 5 mm. **b**, Sensitivity comparisons for the near-infrared images (grey), single-laser (blue) and WIFF (red) intensities for nanosensors implanted as in **a**. Sham stands for gels without a nanosensor; flipped configuration represents a mouse laying on its back with the signal passing through the full thickness of the animal body. The error bars represent standard deviation over $n = 5$ biologically independent samples. **c**, Photograph of an SKH1-E mouse under anaesthesia in the measurement setup with the implanted catheter (i). Scale bar, 1 cm. Near-infrared images of a mouse with a subcutaneously implanted nanosensor ($5 \times 5 \times 2$ mm^3 hydrogel with 20 mg l^{-1} (AC)$_{15}$-SWNTs), demonstrating a change in intensity and nanosensor position before (ii) versus after (iii) injection of 100 μl saline. Scale bar, 5 mm. **d**, Normalized intensity profiles for single-laser and WIFF excitations for the injection in **c** at $t = 0$. **e**, Respective WIFF 2f- and f-intensity components. **f**,**g**, Normalized intensity profiles for single-laser and WIFF excitations (**f**) and extracted concentration (**g**) after an injection of 1 ml riboflavin (300 μM) at $t = 0$ through a catheter in the vicinity of a sensor ($10 \times 10 \times 2$ mm^3 gel with 20 mg l^{-1} (AC)$_{15}$-SWNTs) implanted into the intraperitoneal space of a mouse. **h**, Extracted riboflavin diffusivity. The single-laser excitation was set at 730 nm. The error bars represent standard deviation of the diffusivity fit model. The WIFF system was modulated at 2.5 Hz among 680, 730 and 780 nm. The emission collection was set at >1,100 nm.

In practice, this method error appears to dominate the noise contribution at large implantation depths. Accordingly, WIFF eliminates the need for background subtraction in equation (5), significantly reducing the noise level, as shown above.

To explore the WIFF performance across a broad spectral range, we applied it to ten fluorophores as a proxy of nanosensors that absorb at different wavelengths: TO-PRO-1, Rhodamine 6G, Cy3.5, BODIPY, RFP, Alexa 594, Alexa 700, Alexa 750, Alexa 790 and eFluor 710. Fluorophores were chosen such that their absorption peaks do not overlap with tissue autofluorescence peaks (Fig. 4e). For every fluorophore, we have used a supercontinuum laser with a tunable filter to perform excitation modulation around the respective absorption peak, observing the fluorescence modulation bearing the 2f component (Fig. 4f and Supplementary Fig. 25). Importantly, WIFF improves the SNR compared with the single-laser approach in complex tissues of preserved foetal pigs even in the visible range (Fig. 4g
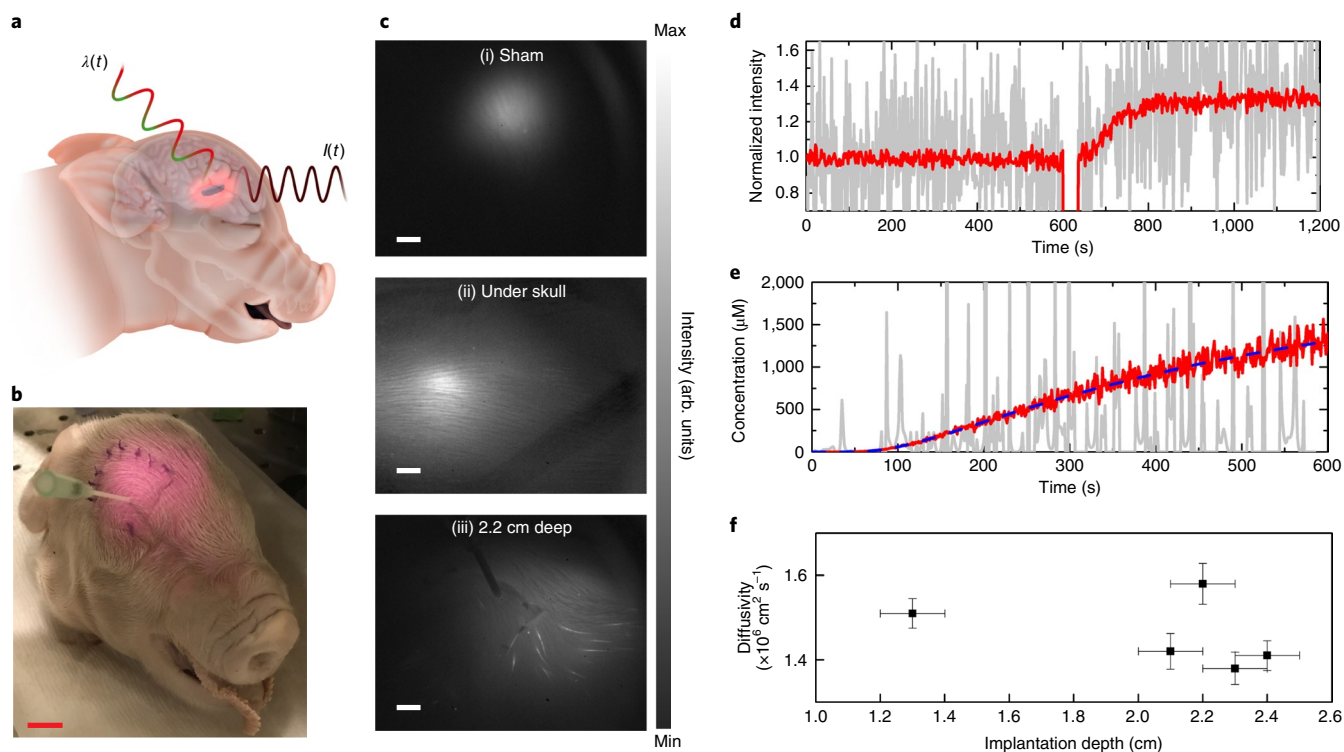
Fig. 6 | Transcranial dynamics of the chemotherapeutic metabolite AIC in porcine brain. a,b, Schematic (**a**) and photograph (**b**) of the head of a preserved foetal pig with an AIC nanosensor ($10 \times 10 \times 2\,mm^3$ hydrogel with $5\,mg\,l^{-1}$ $(GGGT)_3$-SWNTs) implanted into a porcine brain with an unmodified cranium and illuminated with a 730 nm laser. The excitation laser modulation depicted as $\lambda(t)$ translates into the emitted light intensity modulation depicted as $I(t)$. Scale bar, 1 cm. **c**, Near-infrared emission images of implanted nanosensors: sham (implant without a nanosensor) (i), AIC sensor under the skull (ii) and 2.2-cm-deep nanosensor (iii). Scale bars, 5 mm. **d,e**, Normalized intensity profiles for a single laser (black) and WIFF (red) excitations (**d**) and extracted concentration (**e**) after an injection of $200\,\mu l$ AIC (2 mM) at $t = 600\,s$ through the catheter. **f**, Transcranial measurement of AIC diffusivity in the brain. The single-laser excitation was set at 730 nm. The WIFF system was modulated at 2.5 Hz among 680, 730 and 780 nm. The emission collection was set at >1,100 nm. The vertical error bars represent the standard deviation of the diffusivity fit model, whereas the horizontal ones are associated with the method error of nanosensor implantation.

and Supplementary Fig. 26). WIFF also demonstrates improved SNR over extended implantation depths in phantom tissue for various fluorophores (Fig. 4h and Supplementary Fig. 27), corresponding to the ability to work at various levels of autofluorescence relative to a nanosensor signal. The dominant noise in single-laser measurements is dictated by the method error due to the presence of autofluorescence, whereas WIFF successfully eliminates it. Therefore, fluorophores that absorb close to the autofluorescence peak (Alexa 594, BODIPY, eFluor 710 and Alexa 700) demonstrate the highest SNR improvement—with Alexa 594 reaching 52-fold—over the single-laser approach (Fig. 4i).

WIFF aids in measuring tissue permeability in vivo using nanosensors

To evaluate WIFF in vivo, we compared the sensitivity of single-laser excitation with WIFF in live SKH1-E mice (Fig. 5a). Model carbon nanotube sensors embedded in a hydrogel were subcutaneously implanted on the ventral side of the anaesthetized mouse approximately 1 mm under the skin. This geometry simulates the configuration of shallow implantation routinely employed for studies, such as persistent drug release[37], nanosensors for inflammation[23] and glucose sensing[38]. The near-infrared image demonstrates a clear rectangular profile of the hydrogel implant (Fig. 5a). Over $n = 5$ replicas, WIFF allows the high-fidelity detection of signals in two cases (Fig. 5b) compared with sham: (1) when the mouse is lying on its ventral side with the nanosensor facing the detector and (2) when the mouse is flipped to its dorsal side such that the light has an

extraordinarily complex path through the entire body of the animal (at approximately 1.5 cm). The nanosensor signal remains constant during the 40-s-long experiments with 1% noise levels, also indicating the invariance of the G factor to slight animal variation in these replicas. In contrast, measurements with single-laser excitation show ~9% variance between replicas and cannot resolve the latter case (with an unpaired t-test of $p = 0.36$ versus sham). We further compared WIFF with two other techniques used in biomedical sensing. First, near-infrared imaging resolves the implant from the ventral side but not the dorsal side, being confounded by autofluorescence (Supplementary Fig. 28). Second, WIFF also demonstrates a dramatic advantage over spectroscopic measurements with subsequent deconvolution (Supplementary Fig. 29 and Supplementary Table 3), which were previously suggested for autofluorescence elimination[23].

We further illustrate how WIFF handles mechanical artefacts that can be detrimental to optical sensing. In this context, movement and breathing are unavoidable during in vivo experiments. As the control injection of $100\,\mu l$ saline was performed in the vicinity of a subcutaneously implanted nanosensor (as in case (1) mentioned above), the centroid of the implant shifted 2.5 mm, increasing its imaging intensity by 43% compared with that before the injection (Fig. 5c). Measurements with single-laser excitation demonstrated a signal drift of 20% over 600 s as an artefact, whereas WIFF produced a completely stable intensity trace despite these perturbations (Fig. 5d). Here WIFF utilizes the separated background signal as an internal reference. A detailed analysis of the 2f and f components depicts their simultaneous rise, cancelling out such mechanical

artefacts when using equation (4) (Fig. 5e). This self-referencing feature of WIFF is critical for fluorescence assays and nanosensors, allowing users to distinguish between signal artefacts associated with animal movements.

The ultimate goal of fluorescence sensing is to detect analytes in vivo at the implantation point and transmit the signal to the surface of the body. To demonstrate this capability, a nanosensor was implanted into the intraperitoneal space from the ventral side of an SKH1-E mouse. On the injection of 300 μM riboflavin through the catheter implanted near the nanosensor, we observed 17% quenching within an onset time of 51 s after the injection (Fig. 5f), whereas the control showed no response after saline injection (Supplementary Fig. 30). WIFF measurements demonstrate an average noise improvement of ten times over single-laser excitation for $n = 5$ biologically independent replicas, granting the ability to convert the signal into actual concentration values (Supplementary Fig. 31). The extracted concentration trace demonstrates a slow increase characteristic of the diffusion process (Fig. 5g), allowing us to estimate riboflavin diffusivities in the intraperitoneal space of live mice and preserved foetal pigs (Fig. 5h). These types of measurement are critical for many biomedical problems focused on tissue permeability, such as targeted delivery of therapeutics[39] and changes in vascular permeability related to disorders, either as the origin or manifestation of various diseases[40]. For in vivo cases, such measurements are performed with magnetic resonance imaging that have a limited sensitivity of detecting contrast agents[41] and radiolabelling that are associated with safety concerns and high cost[42]. Standard optical methods for tissue permeability, such as Miles assay, fluorescent molecules and labelled bioparticles, are performed either using fibre optics or on dissected tissue slices or extracted organs as these measurements have a limited penetration depth[43]. In our demonstration of applying WIFF to nanosensors, riboflavin perfused into the injection space with the extracted diffusivity values between 0.80×10^{-6} cm² s⁻¹ and 1.60×10^{-6} cm² s⁻¹, closely matching those in the hydrogel (1.04×10^{-6} cm² s⁻¹; Supplementary Fig. 32).

WIFF enables transcranial monitoring of TMZ metabolite in the brain using nanosensors

A long-standing challenge for biosensing is detecting signals through bone tissues as they possess the highest attenuation coefficients in the body[44]. Specifically, a closed anatomy of a skull largely limits the optical monitoring of brain tissue. To illustrate this, consider the problem of glioblastoma treatment. Glioblastoma is the most common and aggressive form of brain tumour in humans[45]. Currently, procedures for glioblastoma patients include surgical resection with subsequent radio- and chemotherapy with TMZ (ref. [46]). TMZ is a pro-drug taken orally that degrades into 5-aminoimidazole-4-carboxamide (AIC) and diazomethane derivatives[47]. Its exact pharmacokinetics within patients differs significantly due to variations in degradation and delivery dynamics, as well as the process of crossing the blood–brain barrier[48]. It is of significant interest to monitor the dose of TMZ and its components delivered to a brain tumour. To date, the most common way of measuring chemotherapeutics is a highly invasive procedure of intracerebral microdialysis with subsequent liquid chromatography analysis[49,50]. Other techniques for pharmacokinetic monitoring include magnetic resonance imaging scans[51] and radiolabelling probes[52]. Optical spectroscopy methods have the ability to non-invasively monitor the brain, but are limited to depths of several millimetres[53,54]. Moreover, these techniques utilize either implanted optical fibres that increase the risk of inflammation[55] or thinned-skull cranial window approaches that have limited timelines until bone regrowth[56]. A method to perform transcranial optical sensing through a full-thickness skull and at significant implantation depths is absent to date.

We demonstrate that WIFF aids in the transcranial monitoring of a nanosensor implanted into the brain of a preserved foetal pig. As an implant, we utilize a selective carbon nanotube sensor for detecting AIC as the metabolic product of TMZ (Supplementary Fig. 33), with a detection limit of 13 μM that is sufficient to resolve clinically relevant drug doses[49]. The implantation procedure results in a sensor embedded up to 2.4 cm deep into the brain covered by a full-thickness cranium and dermis (Fig. 6a,b), commensurate with typical glioblastoma tumour depths[49]. We verified that standard imaging fails to distinguish a deeply implanted nanosensor from a sham, whereas a faint blurred spot was visible when a nanosensor was implanted right beneath the cranium (Fig. 6c). In contrast, WIFF was able to pick a signal from deeply implanted nanosensors, providing SNR enhancement of up to 12 times over the single-laser approach across $n = 5$ biologically independent replicas (Fig. 6d and Supplementary Fig. 34), whereas the control showed no response after saline injection (Supplementary Fig. 35). This improvement turned out to be critical when translating the nanosensor signal into actual concentrations. Although data from the single-laser approach were too noisy to reveal any meaningful information, WIFF successfully captured the dynamics of the injected AIC. The extracted concentration trace demonstrates a slow increase characteristic of the diffusion process (Fig. 6e), allowing us to estimate AIC diffusivities in the brain of preserved foetal pigs at various depths (Fig. 6f). AIC perfused into the injection space with the extracted diffusivity of around 1.4×10^{-6} cm² s⁻¹, in agreement with values from the literature[57].

Conclusions

In this work, we developed WIFF as a means of extending fluorescent nanosensors to the in vivo environment, making the application of deep-tissue sensing possible. WIFF overcomes the limitations of unfavourable intrinsic autofluorescence in the form of method error and mechanical artefacts. This is achieved by an experimental system of cyclic wavelength excitation to separate the emission waveform from the autofluorescence background, lowering the noise levels, as well as to simultaneously use this background as an internal reference, self-correcting for artefacts. As a result, WIFF allows us to detect signals from extraordinarily deep implants of up to 5.5 ± 0.1 cm, demonstrating SNR improvements of up to 52-fold in phantom tissues, chicken tissue, preserved foetal pigs and SKH1-E mouse model (Supplementary Table 4). The method can be readily applied to various fluorescent nanosensors that emit across the entire visible range. WIFF also brings the ability to perform real-time in vivo sensing with high fidelity, as shown for H_2O_2, riboflavin, ascorbic acid and chemotherapeutic drug metabolite nanosensors, in scenarios where conventional optical sensing fails. As an application, we demonstrate that such sensing traces capture the dynamics of local analyte concentrations, revealing diffusion constants related to the important biomedical problem of tissue permeability. Equipped with WIFF, we performed the transcranial monitoring of a metabolite product of TMZ without the need to use optical fibre or perform cranial window insertion, extracting local tissue permeability of the brain tissue. Overall, nanosensors in conjunction with WIFF enable the real-time biochemical monitoring of previously inaccessible in vivo environments, of great interest to the fields of life-sciences research, personalized diagnostics and delivery of targeted therapeutics.

Online content

Any methods, additional references, Nature Research reporting summaries, source data, extended data, supplementary information, acknowledgements, peer review information; details of author contributions and competing interests; and statements of data and code availability are available at https://doi.org/10.1038/s41565-022-01136-x.

References

1. Aron, A. T., Ramos-Torres, K. M., Cotruvo, J. A. & Chang, C. J. Recognition- and reactivity-based fluorescent probes for studying transition metal signaling in living systems. *Acc. Chem. Res.* **48**, 2434–2442 (2015).
2. Lin, V. S., Chen, W., Xian, M. & Chang, C. J. Chemical probes for molecular imaging and detection of hydrogen sulfide and reactive sulfur species in biological systems. *Chem. Soc. Rev.* **44**, 4596–4618 (2015).
3. Cotruvo, J. J. A., Aron, A. T., Ramos-Torres, K. M. & Chang, C. J. Synthetic fluorescent probes for studying copper in biological systems. *Chem. Soc. Rev.* **44**, 4400–4414 (2015).
4. Giuliano, K. A. & Taylor, D. L. Fluorescent-protein biosensors: new tools for drug discovery. *Trends Biotechnol.* **16**, 135–140 (1998).
5. Wolff, M., Wiedenmann, J., Nienhaus, G. U., Valler, M. & Heilker, R. Novel fluorescent proteins for high-content screening. *Drug Discov. Today* **11**, 1054–1060 (2006).
6. Bera, K. et al. Biosensors show the pharmacokinetics of S-ketamine in the endoplasmic reticulum. *Front. Cell. Neurosci.* **13**, 499 (2019).
7. Chen, W.-T., Mahmood, U., Weissleder, R. & Tung, C.-H. Arthritis imaging using a near-infrared fluorescent folate-targeted probe. *Arthritis Res. Ther.* **7**, R310 (2005).
8. Xie, D. Fluorescent dye labeled influenza virus mainly infects innate immune cells and activated lymphocytes and can be used in cell-mediated immune response assay. *J. Immunol. Methods* **343**, 42–48 (2009).
9. Cruz Hernández, J. C. et al. Neutrophil adhesion in brain capillaries reduces cortical blood flow and impairs memory function in Alzheimer's disease mouse models. *Nat. Neurosci.* **22**, 413–420 (2019).
10. Lee, M. H. et al. Toward a chemical marker for inflammatory disease: a fluorescent probe for membrane-localized thioredoxin. *J. Am. Chem. Soc.* **136**, 8430–8437 (2014).
11. Midde, K. et al. Single-cell imaging of metastatic potential of cancer cells. *iScience* **10**, 53–65 (2018).
12. Mehrotra, P. Biosensors and their applications—a review. *J. Oral Biol. Craniofac. Res.* **6**, 153–159 (2016).
13. Sieroń, A. et al. The role of fluorescence diagnosis in clinical practice. *Onco Targets Ther.* **6**, 977–982 (2013).
14. Emanuel, G., Moffitt, J. R. & Zhuang, X. High-throughput, image-based screening of pooled genetic-variant libraries. *Nat. Methods* **14**, 1159–1162 (2017).
15. Koch, M., Symvoulidis, P. & Ntziachristos, V. Tackling standardization in fluorescence molecular imaging. *Nat. Photon.* **12**, 505–515 (2018).
16. Wang, S. et al. Anti-quenching NIR-II molecular fluorophores for in vivo high-contrast imaging and pH sensing. *Nat. Commun.* **10**, 1058 (2019).
17. Zheng, X. et al. Successively activatable ultrasensitive probe for imaging tumour acidity and hypoxia. *Nat. Biomed. Eng.* **1**, 0057 (2017).
18. Unruh, R. M. et al. Preclinical evaluation of poly(HEMA-co-acrylamide) hydrogels encapsulating glucose oxidase and palladium benzoporphyrin as fully implantable glucose sensors. *J. Diabetes Sci. Technol.* **9**, 985–992 (2015).
19. Cash, K. J. & Clark, H. A. In vivo histamine optical nanosensors. *Sensors* **12**, 11922–11932 (2012).
20. Yi, H. et al. M13 phage-functionalized single-walled carbon nanotubes as nanoprobes for second near-infrared window fluorescence imaging of targeted tumors. *Nano Lett.* **12**, 1176–1183 (2012).
21. Yang, J. et al. Ultra-bright near-infrared-emitting HgS/ZnS core/shell nanocrystals for in vitro and in vivo imaging. *J. Mater. Chem. B* **3**, 6928–6938 (2015).
22. Chen, G. et al. (α-NaYbF₄:Tm³⁺)/CaF₂ core/shell nanoparticles with efficient near-infrared to near-infrared upconversion for high-contrast deep tissue bioimaging. *ACS Nano* **6**, 8280–8287 (2012).
23. Iverson, N. M. et al. In vivo biosensing via tissue-localizable near-infrared-fluorescent single-walled carbon nanotubes. *Nat. Nanotechnol.* **8**, 873–880 (2013).
24. Bec, J. et al. In vivo label-free structural and biochemical imaging of coronary arteries using an integrated ultrasound and multispectral fluorescence lifetime catheter system. *Sci. Rep.* **7**, 8960 (2017).
25. Boghossian, A. A. et al. Near-infrared fluorescent sensors based on single-walled carbon nanotubes for life sciences applications. *ChemSusChem* **4**, 848–863 (2011).
26. Zhang, J. et al. Molecular recognition using corona phase complexes made of synthetic polymers adsorbed on carbon nanotubes. *Nat. Nanotechnol.* **8**, 959–968 (2013).
27. Salem, D. P. et al. Ionic strength-mediated phase transitions of surface-adsorbed DNA on single-walled carbon nanotubes. *J. Am. Chem. Soc.* **139**, 16791–16802 (2017).
28. Rieker, G. B., Jeffries, J. B. & Hanson, R. K. Measurements of high-pressure CO_2 absorption near 2.0 μm and implications on tunable diode laser sensor design. *Appl. Phys. B* **94**, 51–63 (2009).
29. Shimada, T. et al. Pharmacokinetic advantage of intraperitoneal injection of docetaxel in the treatment for peritoneal dissemination of cancer in mice. *J. Pharm. Pharmacol.* **57**, 177–181 (2005).
30. Lu, Z., Wang, J., Wientjes, M. G. & Au, J. L. S. Intraperitoneal therapy for peritoneal cancer. *Future Oncol.* **6**, 1625–1641 (2010).
31. Zempleni, J., Galloway, J. R. & McCormick, D. B. Pharmacokinetics of orally and intravenously administered riboflavin in healthy humans. *Am. J. Clin. Nutr.* **63**, 54–66 (1996).
32. Park, M. et al. Measuring the accessible surface area within the nanoparticle corona using molecular probe adsorption. *Nano Lett.* **19**, 7712–7724 (2019).
33. Koman, V. B., von Moos, N. R., Santschi, C., Slaveykova, V. I. & Martin, O. J. F. New insights into ROS dynamics: a multi-layered microfluidic chip for ecotoxicological studies on aquatic microorganisms. *Nanotoxicology* **10**, 1041–1050 (2016).
34. Loock, H.-P. & Wentzell, P. D. Detection limits of chemical sensors: applications and misapplications. *Sens. Actuators B* **173**, 157–163 (2012).
35. Krasnovsky, A. Jr. & Kovalev, Y. Spectral and kinetic parameters of phosphorescence of triplet chlorophyll a in the photosynthetic apparatus of plants. *Biochemistry* **79**, 349–361 (2014).
36. Inoue, Y., Izawa, K., Kiryu, S., Tojo, A. & Ohtomo, K. Diet and abdominal autofluorescence detected by in vivo fluorescence imaging of living mice. *Mol. Imaging* **7**, 7290.2008.0003 (2008).
37. Kim, H., Park, H. & Lee, S. J. Effective method for drug injection into subcutaneous tissue. *Sci. Rep.* **7**, 9613 (2017).
38. Mortellaro, M. & DeHennis, A. Performance characterization of an abiotic and fluorescent-based continuous glucose monitoring system in patients with type 1 diabetes. *Biosens. Bioelectron.* **61**, 227–231 (2014).
39. Rosenblum, D., Joshi, N., Tao, W., Karp, J. M. & Peer, D. Progress and challenges towards targeted delivery of cancer therapeutics. *Nat. Commun.* **9**, 1410 (2018).
40. Fukui, H. Increased intestinal permeability and decreased barrier function: does it really influence the risk of inflammation? *Inflamm. Intest. Dis.* **1**, 135–145 (2016).
41. Penet, M.-F. et al. Applications of molecular MRI and optical imaging in cancer. *Future Med. Chem.* **2**, 975–988 (2010).
42. Gambhir, S. S. Molecular imaging of cancer with positron emission tomography. *Nat. Rev. Cancer* **2**, 683–693 (2002).
43. Ibla, J. C. & Khoury, J. in *Cell–Cell Interactions: Methods and Protocols* Vol. 1066 (ed. Colgan, S. P.) 111–117 (Humana Press, 2006).
44. Jacques, S. L. Optical properties of biological tissues: a review. *Phys. Med. Biol.* **58**, R37–R61 (2013).
45. Hambardzumyan, D. & Bergers, G. Glioblastoma: defining tumor niches. *Trends Cancer* **1**, 252–265 (2015).
46. Stupp, R. et al. Radiotherapy plus concomitant and adjuvant temozolomide for glioblastoma. *N. Engl. J. Med.* **352**, 987–996 (2005).
47. Friedman, H. S., Kerby, T. & Calvert, H. Temozolomide and treatment of malignant glioma. *Clin. Cancer Res.* **6**, 2585–2597 (2000).
48. Holohan, C., Van Schaeybroeck, S., Longley, D. B. & Johnston, P. G. Cancer drug resistance: an evolving paradigm. *Nat. Rev. Cancer* **13**, 714–726 (2013).
49. Portnow, J. et al. The neuropharmacokinetics of temozolomide in patients with resectable brain tumors: potential implications for the current approach to chemoradiation. *Clin. Cancer Res.* **15**, 7092–7098 (2009).
50. Liu, H.-L. et al. Pharmacodynamic and therapeutic investigation of focused ultrasound-induced blood-brain barrier opening for enhanced temozolomide delivery in glioma treatment. *PLoS ONE* **9**, e114311 (2014).
51. Kato, Y., Holm, D. A., Okollie, B. & Artemov, D. Noninvasive detection of temozolomide in brain tumor xenografts by magnetic resonance spectroscopy. *Neuro. Oncol.* **12**, 71–79 (2010).
52. Arı, K. et al. ⁹⁹ᵐTc(I) carbonyl-radiolabeled lipid based drug carriers for temozolomide delivery and bioevaluation by in vitro and in vivo. *Radiochim. Acta* **107**, 1185–1193 (2019).
53. Torricelli, A. et al. Time domain functional NIRS imaging for human brain mapping. *NeuroImage* **85**, 28–50 (2014).
54. Strangman, G. E., Li, Z. & Zhang, Q. Depth sensitivity and source-detector separations for near infrared spectroscopy based on the Colin27 brain template. *PLoS ONE* **8**, e66319 (2013).
55. Wellman, S. M. & Kozai, T. D. Y. Understanding the inflammatory tissue reaction to brain implants to improve neurochemical sensing performance. *ACS Chem. Neurosci.* **8**, 2578–2582 (2017).
56. Dorand, R. D., Barkauskas, D. S., Evans, T. A., Petrosiute, A. & Huang, A. Y. Comparison of intravital thinned skull and cranial window approaches to study CNS immunobiology in the mouse cortex. *IntraVital* **3**, e29728 (2014).
57. Wen, Q. et al. Association of diffusion and anatomic imaging parameters with survival for patients with newly diagnosed glioblastoma participating in two different clinical trials. *Transl. Oncol.* **8**, 446–455 (2015).

Methods

Tissue autofluorescence measurements. The excitation–emission maps of the tissue samples were obtained using excitation from a supercontinuum source (EXW-12, NKT Photonics) with a tunable filter (LLTF CONTRAST-SR-VIS-HP8, Photon etc.) on an inverted microscope (AxioVision, Zeiss), using a ×20 air objective coupled to a near-infrared camera (OMA V InGaAs, Princeton Instruments) through a spectrometer (SP-2500, PI Acton) and using WinSpec software (version 2.4; Princeton Instruments). The typical integration time was 60 s for one excitation wavelength with several milliwatts of power on the sample. The setup was intensity calibrated.

Preparation of carbon nanotube sensors. Raw HiPCO SWNTs were purchased from NanoIntegris (Lot #HR27-104). All the single-stranded DNA oligonucleotides were purchased from Integrated DNA Technologies. Carbon nanotube suspension for H_2O_2 (ascorbic acid) detection was prepared by mixing 1.00 mg $(GT)_{15}$ $((ACCA)_7)$ oligonucleotide and 0.25 mg HiPCO SWNT. All the suspensions were diluted to 1 ml of 50 mM NaCl. For riboflavin detection, 1 mg $(AC)_{15}$ oligonucleotide was used instead. For AIC detection, 2 mg $(GGGT)_3$ oligonucleotide was used instead. The mixture was sonicated with a 3 mm probe tip (Cole-Parmer) for 20 min at 40% amplitude in an ice bath. The sample was then centrifuged twice at 16,000 g for 90 min each to remove unsuspended SWNT bundles. The concentration of SWNT suspension was determined using its absorbance at 632 nm and extinction coefficient of 0.036 mg^{-1} l^{-1} cm^{-1}. Unless stated otherwise, we excited the (9,4) and (8,6) chiralities in a sample with absorption peaks at 720 and 735 nm, respectively, as the model sensor. Carbon nanotubes were selected as they are routinely used as near-infrared nanosensors[25,58,59] because of their single-molecule sensitivity[60,61], corona-modulated selectivity[26,62,63] and resistance to photobleaching[25].

Phantom tissue preparation. A phantom tissue was fabricated with parameters close to those of a mouse brain as it was found to have the second-highest autofluorescence level after the stomach, making the problem of autofluorescence relevant when dealing with such tissue. Additionally, brain sensing poses an important biomedical problem. To simulate light propagation in such tissue, we have taken approximate values from another study for absorption and scattering coefficients[44]: $\mu_{abs} = 0.02$ cm^{-1} and $\mu_{sca} = 17.00$ cm^{-1} at $\lambda_{exc} = 730$ nm excitation wavelength, and $\mu_{abs} = 0.09$ cm^{-1} and $\mu_{sca} = 2.00$ cm^{-1} at $\lambda_{em} = 1,150$ nm emission wavelength.

Tissue absorption in the region of interest is dominated by water. Hence, a water solution closely mimics the absorption properties of brain tissue. According to another study[64], adding 0.7% intralipid allows us to achieve $\mu_{sca} = 17$ cm^{-1} at 730 nm and 2 cm^{-1} at 1,150 nm. The phantom tissue was calibrated by matching the experimental measurement to previously established Monte Carlo simulations (Supplementary Fig. 21). Autofluorescence was introduced by adding 0.15 mg l^{-1} chlorophyll, which results in autofluorescence intensity similar to that of the brain when excited at 730 nm. The appropriate G factor was measured and taken into account as described below, with values summarized in Supplementary Table 1. The mixture of chlorophyll and intralipid was complemented by 1% agarose heated to 90 °C to dissolve agarose and slowly cooled down to room temperature, which solidified the mixture into a gel. The mixtures were moulded in three-dimensional printed forms of various thicknesses.

The chicken breast tissue was purchased frozen from the supermarket and was not found to have any autofluorescence. To recreate the properties of living tissues, we soaked the tissue into 0.15 mg l^{-1} chlorophyll solution overnight. For Monte Carlo simulations, the following parameters were estimated: $\mu_{abs} = 0.02$ cm^{-1} and $\mu_{sca} = 12.00$ cm^{-1} at $\lambda_{exc} = 730$ nm, and $\mu_{abs} = 0.08$ cm^{-1} and $\mu_{sca} = 1.90$ cm^{-1} at $\lambda_{em} = 1,150$ nm.

The foetal pigs (Nasco, LS03783) were purchased preserved in propylene glycol. A 10×10 mm^2 piece of hydrogel was implanted into the intraperitoneal space through a ventral incision. A 2.5 inch catheter was implanted in the intraperitoneal space through the same incision. The abdominal muscles and skin were closed using sutures. During imaging, 3 ml of 1 mM riboflavin (or saline for controls) was injected into the intraperitoneal space through the catheter after collecting the fluorescence baseline for 10 min. For transcranial measurements, the skin and muscle over the cranial midline of the 13–16 inch preserved foetal pigs (Nasco, LS03791) were dissected (~2×2 cm^2) to reveal the skull. Approximately 1×1 cm^2 section of the skull near the eye socket was removed. The dura underneath the nearby still-intact skull was gently dissected blindly and bluntly. A hydrogel with an encapsulated SWNT nanosensor was implanted into the space where the dura was removed. A 2.5 inch catheter was implanted in the intracranial space through the same incision. The cranial muscles and skin were closed using nylon sutures. The pigs were decapitated with a scalpel blade to assist in the imaging. Compared with live foetal pigs, the preserved ones might have fainter autofluorescence background, underestimating the WIFF performance. Indeed, according to Fig. 4i, stronger autofluorescence leads to higher SNR improvements. Live foetal pigs will be the topic of future research. A specific amount of analyte was chosen to make sure to fill the space where a sensor was implanted, whereas a high enough concentration was used to ensure reasonable diffusion times.

Monte Carlo simulations. To simulate light propagation through a tissue, we use a probabilistic approach based on a Monte Carlo scheme[65]. Incident light is treated as wavepackets instead of single photons to simulate absorption along the optical path. Between two successive scattering events, the wavepacket travels in a straight line losing its energy through absorption of the tissue, characterized by μ_{abs}, according to Beer–Lambert's law. The mean free path of light l_{free} between two successive scattering events is found as $l_{free} = 1/(\mu_{sca}(1-g))$, where $g = <\cos\theta>$ is the average scattering angle or anisotropy parameter (taken to be 0.9 in this work). The distance between two consecutive scattering events, p, follows the random distribution expressed by $p = -l_{free}\log\Sigma$, where Σ is sampled uniformly between 0 and 1. When a wavepacket is scattered, it changes its direction with the scattering probability function $q(\theta)$ given by the Henyey–Greenstein distribution:

$$q(\theta) = \frac{1-g^2}{4\pi(1+g^2-2g\cos\theta)^{3/2}}.$$

We sequentially trace wavepackets until they reach the boundaries of the box simulation (we take a $10 \times 10 \times 10$ cm^3 box) or until the energy decreases by a factor of 10^{12}. The simulation box is divided into cells ($0.1 \times 0.1 \times 0.1$ cm^3), recording the absorbed energy from every wavepacket. To achieve a reasonable approximation of a realistic system, we launch 10^8 wavepackets for every simulation. The process of light emission is simulated in a separate code with a wavepacket originating in every simulation cell. The sensor signal is determined as the light intensity reaching the surface of the tissue multiplied by the quantum yield and excitation intensity of light absorbed by the cells where the sensor is implanted. Tissue autofluorescence is determined as the light intensity reaching the surface of the tissue multiplied by the quantum yield taken from the experiment and excitation intensity of light absorbed by all the cells of the tissue except where the sensor is implanted.

Optical measurements. Optical measurements were performed in the reflection configuration. A laser (730 nm; LDX-3430-730, LDX Optronics) was focused using cylindrical and spherical lenses onto the tissue sample with an 800 nm short-pass filter to cut out the laser tail. The laser was controlled by current and temperature modules (Thorlabs). The reflected signal was collected through a dichroic mirror (850 nm long pass) and 1,000 nm and 1,100 nm long-pass filters using a collimating lens onto a near-infrared photodetector (PDF10C, Thorlabs) measured using the LJStreamM software (version 1.06; LabJack). The spectral response was measured to ensure that no signature of laser reflection was present, which is often confused with autofluorescence. A stack of multiple band-pass filters (with a typical optical density of 6–7) was necessary to efficiently filter out signals that are 10–12 orders of magnitude weaker compared with the incident light. A slanted configuration between filters was introduced to ensure the absence of the cavity effect that would otherwise occur between reflective surfaces, decreasing the filtering capabilities. The optical signal was intensity modulated by a mechanical chopper (SR540, Stanford Research Systems) at 100 Hz and the modulated signal was read out by the lock-in amplifier (SR830, Stanford Research Systems). Note that this is orthogonal modulation targeted at decreasing the read-out noise compared with WIFF that modulates the signal in the excitation frequency to eliminate the need for background measurements. The detector was intensity calibrated, which matched very well with the values provided by the supplier (photoresponsivity, $R = 1$ A W^{-1}; gain, 10^8 kV A^{-1}). The detector operated at 500 Hz collection frequency with post-measurement co-adding. For experiments with implants, the sensor signal was calculated as the difference between two measurements from a sample with and without a sensor (background). The background was replicated $n = 5$ times. Typically, a standard variation of 6–10% was observed between the background replicas, associated with tissue movement during handling.

To understand the contributions of various noise components, we studied the photodetector behaviour (Supplementary Fig. 24). The noise r.m.s. value was measured as a standard deviation of the signal under a given condition over 100 s. On increasing the illumination power, the photodetector noise increases with the shot noise. Finding the shot noise to reach 5 pW before saturating the detector ($t = 0.002$ s), we determined the read-noise contribution to be 39 pW. The latter consists of the so-called white and pink components. The application of a lock-in amplifier reduces the read noise, decreasing the pink noise, to the white noise with r.m.s. value of 4 pW at 100 Hz. Finally, the SNR can also be improved at the expense of integration time: the signal grows faster than noise as t increases (Supplementary Fig. 24).

To perform wavelength modulation, we added two lasers to the above system: 680 nm (LDX-3230-680) and 780 nm (LDX-3215-760), both from LDX Optronics. Mechanical shutters (Thorlabs) were programmed to open in a sequential order using Kinesis software (version 1.14; Thorlabs). Special care was taken to align the excitation paths of the three lasers to illuminate the same area on the sample. The incident power on the sample was just below the damage threshold (~300 mW cm^{-2}) with an illumination area of 10×10 cm^2 and fluorescence was collected in the 1,100–1,300 nm spectral range. In this work, we estimate carbon nanotubes' quantum efficiency to be 1%; typically, the implant had 0.01 optical density at 730 nm excitation, whereas fluorescent light was collected with 10% efficiency based on the solid-angle calculations. In cases when autofluorescence is weak compared with the signal (specific or thin tissues), the f component of the signal was mostly determined by the sensor and not the background. Hence, the technique cannot use the f component as a reference point in this case.

Unless stated otherwise, WIFF modulation is performed at $f = 2.5$ Hz. Next, the raw fluorescent intensity trace is split in 2 s segments that are individually processed using fast Fourier transform (FFT). The single-sided amplitude spectrum is calculated using 500 Hz as the sampling frequency, corresponding to that of the detector. The intensities corresponding to a specific frequency, such as $P_s(f)$ and $P_s(2f)$, are then directly extracted for a given time point (Supplementary Figs. 15 and 16) using MATLAB R2019a (MathWorks). Before sensor implantation, tissue autofluorescence is first measured. For this, WIFF is performed, aiming the excitation beam around the anticipated position of sensor implantation. The ratio between $P_b(f)$ and $P_b(2f)$ is then used to find the G factor (equation (3)). After sensor implantation, the laser intensities are tuned to achieve the highest component $P_s(2f)$ (Supplementary Note 3) to correct for tissue absorption effects. Knowing the initial G factor, the updated G factor is recalculated using a simple FFT according to the updated excitation powers.

For dyes emitting in the visible range, excitation was performed using the supercontinuum source and tunable filter (as above). The detection was performed using a Si photodetector (APD120A, Thorlabs) that was intensity calibrated. Dye solutions were contained in a chamber made of two glass slides and an O-ring sealed with vacuum grease ($\sim 5 \times 5 \times 2$ mm³ total volume). Chambers were implanted into the phantom tissue. Due to different ratios between the fluorescence intensity and autofluorescence, various dyes were implanted at different depths. The following dyes were implanted at 1 cm: TO-PRO-1, Rhodamine 6G, Alexa 700 and eFluor 710. The following dyes were implanted at 1.5 cm: Alexa 750 and Alexa 790. The following dyes were implanted at 0.5 cm depth: Alexa 594, BODIPY and RFP. The Cy3.5 dye was implanted at 0.5 cm depth in the phantom tissue that has reduced chlorophyll content (0.015 mg l⁻¹). For dyes implanted at 0.5 cm, SNR at 1 cm was numerically estimated using the respective values measured at 0.5 cm and Monte Carlo simulations. The optical properties of the phantom tissue were matched to those of the brain tissue at the wavelength of excitation by following the procedures described above. A needle was inserted through an O-ring to deliver analytes into the chamber. The following dye concentrations were used in 10 μM: TO-PRO-1, Rhodamine 6G, Cy3.5, BODIPY, RFP and Alexa 594; Alexa 750, Alexa 790 and eFluor 710 were used in 2 μM. Due to the limited spectral window available for excitation, the dye absorption at the excitation sidelines were not always identical (Supplementary Fig. 25), which slightly reduced the efficiency of the modulation scheme and lowered the $P_s(2f)/P_s$ ratio.

Standoff imaging. The wide-field-of-view imaging setup uses a Princeton Instruments OMA V InGaAs detector to capture a two-dimensional image of an SKH1-E mouse with the hydrogel. The detector is cooled to –100 °C using liquid N₂. The detector was affixed with a Nikon AF Micro-Nikkor 60 mm f/2.8D lens to focus the image. An FELH 900 nm long-pass filter (Thorlabs) was placed between the lens and detector to filter out the excitation light. The nanotube-embedded hydrogel was excited using a 785 nm Invictus laser with a power density of 20 mW cm⁻². The images obtained by this setup were corrected by subtracting the dark current of the detector at the given exposure time. The typical integration time was 1 s.

Hydrogel preparation. A biocompatible hydrogel that can be easily handled and implanted at a desired location within an animal represents an important form factor that minimizes variation in the localization of the carbon nanotube. Nanotube-embedded hydrogels were prepared using polyethylene glycol diacrylate from Alfa Aesar using a polyethylene glycol chain length of 8,000 Da (PEG8000DA). The ultraviolet (UV)-triggered initiator was 2-hydroxy-4′-(2-hydroxyethoxy)-2-methylpropiophenone (Sigma-Aldrich) and was dissolved in a stock solution of 7 mg ml⁻¹ in water before polymerization. The hydrogel precursor solution had a final concentration of polymer 10% (w/v), 20 mg l⁻¹ SWNT and 2.5% (v/v) saturated initiator solution dissolved in 1× phosphate buffered saline (PBS). The hydrogel precursor solution is held under a flowing N₂ atmosphere for 30 min to remove the dissolved oxygen. After degassing, the solution is pipetted into glass moulds and returned to the N₂ atmosphere. The moulds are then exposed to 365 nm UV light (UVP Blak-Ray XX-15BLB) for 45 min to polymerize. Afterwards, the hydrogels were removed from the moulds and left to incubate in ×1 PBS overnight to remove any unreacted monomers to free-floating SWNTs. Then, the 1× PBS solution was exchanged to a fresh solution and the hydrogels were ready to use.

Animal work. All the performed procedures were approved by the Committee on Animal Care and the Division of Comparative Medicine at the Massachusetts Institute of Technology. The mice used for this study are female SKH1-E mice purchased from Charles River Laboratories. The SKH1-E line is a nude immunocompetent mouse line to simplify the imaging of fluorescent implants. All the mice are purchased at six weeks old and the mice used in this study are between 8 and 24 weeks of age. For tissue autofluorescence, the mice were killed using CO₂ asphyxiation and the tissues of interest were resected. Note that autofluorescence fades away within a couple of hours after the animal is killed. For in vivo implantations, hydrogels were sterilized before implantation by

illumination with UV light for 30 min. Either a 10×10 mm² piece of hydrogel was implanted into the intraperitoneal space through a ventral incision or a 5×5 mm² piece was subcutaneously implanted. A 2.5 inch catheter was implanted in the intraperitoneal space through the same incision. The abdominal muscles and skin were closed using sutures. Before the operation, the mouse was anaesthetized using 2% isoflurane gas and held under for the remainder of the surgery and subsequent imaging. Additionally, analgesics were administered before implantation. During imaging, 1 ml of 300 μM riboflavin (or saline for controls) was injected into the intraperitoneal space through the catheter after collecting the fluorescent baseline for 10 min. The data were collected for 10 min post-injection.

Reporting Summary. Further information on research design is available in the Nature Research Reporting Summary linked to this article.

Data availability
Source data are available via Zenodo at https://doi.org/10.5281/zenodo.6049452. The data that support the findings of this study are available in the paper and Supplementary Information. All other data are available from the corresponding author upon reasonable request.

References
58. Landry, M. P. et al. Experimental tools to study molecular recognition within the nanoparticle corona. *Sensors* **14**, 16196–16211 (2014).
59. Hendler-Neumark, A. & Bisker, G. Fluorescent single-walled carbon nanotubes for protein detection. *Sensors* **19**, 5403 (2019).
60. Landry, M. P. et al. Single-molecule detection of protein efflux from microorganisms using fluorescent single-walled carbon nanotube sensor arrays. *Nat. Nanotechnol.* **12**, 368–377 (2017).
61. Jin, H. et al. Detection of single-molecule H₂O₂ signalling from epidermal growth factor receptor using fluorescent single-walled carbon nanotubes. *Nat. Nanotechnol.* **5**, 302–309 (2010).
62. Bisker, G. et al. Insulin detection using a corona phase molecular recognition site on single-walled carbon nanotubes. *ACS Sens.* **3**, 367–377 (2018).
63. Bisker, G. et al. Protein-targeted corona phase molecular recognition. *Nat. Commun.* **7**, 10241 (2016).
64. Flock, S. T., Jacques, S. L., Wilson, B. C., Star, W. M. & van Gemert, M. J. C. Optical properties of intralipid: a phantom medium for light propagation studies. *Lasers Surg. Med.* **12**, 510–519 (1992).
65. Koman, V. B., Santschi, C. & Martin, O. J. F. Maximal absorption regime in random media. *Opt. Express* **24**, A1306–A1320 (2016).

Author contributions
V.B.K. and M.S.S. conceived the idea and planned the experiments with the assistance of N.A.B., X.J. and F.T.N. V.B.K. developed the experimental setup, performed the in vitro experiments and analysed the data with the assistance of D.K., F.T.N., M.A.L., G.B. and J.D. F.T.N. and V.B.K. performed the tissue autofluorescence studies. N.A.B. and X.J. performed the ex vivo and in vivo experiments with the assistance of V.B.K. V.B.K. and M.S.S. wrote the manuscript with inputs from all the authors. All the authors contributed to discussions regarding the research.

Competing interests
The authors declare no competing interests.

Additional information
Supplementary information The online version contains supplementary material available at https://doi.org/10.1038/s41565-022-01136-x.

Correspondence and requests for materials should be addressed to Michael S. Strano.

Peer review information *Nature Nanotechnology* thanks Yun-Sheng Chen and Fan Zhang for their contribution to the peer review of this work.

Reprints and permissions information is available at www.nature.com/reprints.

nature portfolio

Corresponding author(s): Michael Strano

Last updated by author(s): Apr 6, 2022

Reporting Summary

Nature Portfolio wishes to improve the reproducibility of the work that we publish. This form provides structure for consistency and transparency in reporting. For further information on Nature Portfolio policies, see our Editorial Policies and the Editorial Policy Checklist.

Statistics

For all statistical analyses, confirm that the following items are present in the figure legend, table legend, main text, or Methods section.

n/a	Confirmed	
☐	☒	The exact sample size (*n*) for each experimental group/condition, given as a discrete number and unit of measurement
☐	☒	A statement on whether measurements were taken from distinct samples or whether the same sample was measured repeatedly
☐	☒	The statistical test(s) used AND whether they are one- or two-sided *Only common tests should be described solely by name; describe more complex techniques in the Methods section.*
☒	☐	A description of all covariates tested
☒	☐	A description of any assumptions or corrections, such as tests of normality and adjustment for multiple comparisons
☐	☒	A full description of the statistical parameters including central tendency (e.g. means) or other basic estimates (e.g. regression coefficient) AND variation (e.g. standard deviation) or associated estimates of uncertainty (e.g. confidence intervals)
☒	☐	For null hypothesis testing, the test statistic (e.g. *F*, *t*, *r*) with confidence intervals, effect sizes, degrees of freedom and *P* value noted *Give P values as exact values whenever suitable.*
☒	☐	For Bayesian analysis, information on the choice of priors and Markov chain Monte Carlo settings
☒	☐	For hierarchical and complex designs, identification of the appropriate level for tests and full reporting of outcomes
☒	☐	Estimates of effect sizes (e.g. Cohen's *d*, Pearson's *r*), indicating how they were calculated

Our web collection on statistics for biologists contains articles on many of the points above.

Software and code

Policy information about availability of computer code

Data collection	Winspec software version 2.4 (Princeton Instruments) Kinesis software version 1.14 (Thorlabs) LJStreamM software version 1.06 (LabJack)
Data analysis	Matlab R2019a (Mathworks)

For manuscripts utilizing custom algorithms or software that are central to the research but not yet described in published literature, software must be made available to editors and reviewers. We strongly encourage code deposition in a community repository (e.g. GitHub). See the Nature Portfolio guidelines for submitting code & software for further information.

Data

Policy information about availability of data

All manuscripts must include a data availability statement. This statement should provide the following information, where applicable:

- Accession codes, unique identifiers, or web links for publicly available datasets
- A description of any restrictions on data availability
- For clinical datasets or third party data, please ensure that the statement adheres to our policy

The data that support the findings of this study are available within the paper and the Supplementary Information. Source data have been deposited online at Zenodo. Other relevant data are available from the corresponding authors on reasonable request.

Field-specific reporting

Please select the one below that is the best fit for your research. If you are not sure, read the appropriate sections before making your selection.

☒ Life sciences   ☐ Behavioural & social sciences   ☐ Ecological, evolutionary & environmental sciences

For a reference copy of the document with all sections, see nature.com/documents/nr-reporting-summary-flat.pdf

Life sciences study design

All studies must disclose on these points even when the disclosure is negative.

Sample size	Power analysis was employed to determine sample sizes. Sample sizes were chosen based on the variability of preliminary experiments, with a minimum of n = 3 independent biological replicates to ensure reproducibility of the results. They have been explicitly indicated in the respective table and figure legend.
Data exclusions	No data were excluded.
Replication	We confirm that all attempts at replication were successful. The experiments were performed at least in triplicates with specific conditions given in the text.
Randomization	For animal experiments, mice were randomly allocated into each treatment group. All other experiments involved randomized samples.
Blinding	Due to the proof-of-concept developmental nature of this study, true blinding of experiments was not performed. However, data collection and analyses for some experiments were performed by separate individuals. In some cases, these collectors/analyzers were not aware which samples corresponded to which experimental groups at the time of data collection and analysis.

Reporting for specific materials, systems and methods

We require information from authors about some types of materials, experimental systems and methods used in many studies. Here, indicate whether each material, system or method listed is relevant to your study. If you are not sure if a list item applies to your research, read the appropriate section before selecting a response.

Materials & experimental systems

n/a	Involved in the study
☒	☐ Antibodies
☒	☐ Eukaryotic cell lines
☒	☐ Palaeontology and archaeology
☐	☒ Animals and other organisms
☒	☐ Human research participants
☒	☐ Clinical data
☒	☐ Dual use research of concern

Methods

n/a	Involved in the study
☒	☐ ChIP-seq
☒	☐ Flow cytometry
☒	☐ MRI-based neuroimaging

Animals and other organisms

Policy information about studies involving animals; ARRIVE guidelines recommended for reporting animal research

Laboratory animals	The mice used for this study are female SKH1-E mice purchased from Charles River Laboratories. The SKH1-E line is a nude immunocompetent mouse line to simplify imaging of fluorescent implants. All mice are purchased at 6 weeks old and any mice used in this study are between 8-24 weeks of age. The light cycle is 12/12- lights go on at 7:00am and off at 7:00pm. The Temp is 68-70 degrees, but the humidity's have a larger range,(30-70%).
Wild animals	The study did not involve wild animals.
Field-collected samples	The study did not involve samples collected from the field.
Ethics oversight	All animal experiments were approved by the Committee on Animal Care (CAC) and the Division of Comparative Medicine (DCM) at the Massachusetts Institute of Technology.

Note that full information on the approval of the study protocol must also be provided in the manuscript.